Article

A Histogram-Based Low-Complexity Approach for the Effective Detection of COVID-19 Disease from CT and X-ray Images

Michele Scarpiniti *[iD]**, Sima Sarv Ahrabi** [iD]**, Enzo Baccarelli** [iD]**, Lorenzo Piazzo** [iD] **and Alireza Momenzadeh** [iD]

Department of Information Engineering, Electronics and Telecommunications (DIET), Sapienza University of Rome, Via Eudossiana 18, 00185 Rome, Italy; sima.sarvahrabi@uniroma1.it (S.S.A.); enzo.baccarelli@uniroma1.it (E.B.); lorenzo.piazzo@uniroma1.it (L.P.); alireza.momenzadeh@uniroma1.it (A.M.)
* Correspondence: michele.scarpiniti@uniroma1.it; Tel.: +39-06-44585869

Abstract: The global COVID-19 pandemic certainly has posed one of the more difficult challenges for researchers in the current century. The development of an automatic diagnostic tool, able to detect the disease in its early stage, could undoubtedly offer a great advantage to the battle against the pandemic. In this regard, most of the research efforts have been focused on the application of Deep Learning (DL) techniques to chest images, including traditional chest X-rays (CXRs) and Computed Tomography (CT) scans. Although these approaches have demonstrated their effectiveness in detecting the COVID-19 disease, they are of huge computational complexity and require large datasets for training. In addition, there may not exist a large amount of COVID-19 CXRs and CT scans available to researchers. To this end, in this paper, we propose an approach based on the evaluation of the histogram from a common class of images that is considered as the target. A suitable inter-histogram distance measures how this target histogram is far from the histogram evaluated on a test image: if this distance is greater than a threshold, the test image is labeled as anomaly, i.e., the scan belongs to a patient affected by COVID-19 disease. Extensive experimental results and comparisons with some benchmark state-of-the-art methods support the effectiveness of the developed approach, as well as demonstrate that, at least when the images of the considered datasets are homogeneous enough (i.e., a few outliers are present), it is not really needed to resort to complex-to-implement DL techniques, in order to attain an effective detection of the COVID-19 disease. Despite the simplicity of the proposed approach, all the considered metrics (i.e., accuracy, precision, recall, and F-measure) attain a value of 1.0 under the selected datasets, a result comparable to the corresponding state-of-the-art DNN approaches, but with a remarkable computational simplicity.

Keywords: inter-histogram distance; Computed Tomography (CT); Chest X-ray (CXR); COVID-19; pneumonia; anomaly detection

1. Introduction

The novel Severe Acute Respiratory Syndrome Coronavirus 2 (SARS-CoV-2) is the cause of one of the worst pandemic of this century: the Coronavirus Disease 2019 (or, simply, COVID-19) [1]. COVID-19 is responsible for illness in the respiratory system, with common symptoms, such as fever and cough, and can also lead to severe pneumonia, an infection that causes a severe inflammation in the lungs' air sacs, which are responsible for the oxygen exchange [2].

However, many studies have highlighted that the Novel COVID-19 Pneumonia (NCP) is different from other viral (Common) Pneumonia (CP) [3]. In this regard, some works have shown that cases of NCP tend to affect the entire lung, unlike common diseases that are limited to small regions [3,4]. Pneumonia caused by the COVID-19 shows a typical hazy patch on the outer edges of the lungs.

Due to the seriousness of possible consequences of COVID-19, early detection of the disease is vital [2]. Currently, the COVID-19 screening is commonly based on the

real-time Reverse Transcription-Polymerase Chain Reaction (rRT-PCR). This technique has demonstrated a sufficiently high specificity; however, its sensitivity is relatively low in diagnosing COVID-19 [5].

This problem has motivated researchers to investigate the role of medical imaging as a valid tool for performing non-invasive medical diagnoses [6]. Among the different techniques, conventional Chest X-Rays (CXRs) and Computed Tomography (CT) [7] have assumed a very important role in detecting COVID-19 [8–10].

Although CXRs appear diagnostically an effective means of identifying the symptoms of COVID-19, in comparison with chest CT scans, their sensitivity is generally low for pulmonary diseases [11]. Therefore, CXRs make the accurate diagnosis of COVID-19 pneumonia more challenging in comparison with chest CT scans [11]. However, it is not always easy for radiologists to analyze and interpret the CT scans. In addition, in order to reduce the dose of radiation and avoid harmful consequences (such as tumors), it is preferable to perform scans with a low emission of radiation [4]. In this case, the scanned images often have a degraded quality (such as blur, background noise, and low contrast), which makes it ambiguous and difficult to put an accurate interpretation on CT scans [12].

In order to attempt to effectively sort out the above problems, the efforts of the research community are, for the most part, focused on exploiting Artificial Intelligence (AI) approaches for implementing automatic image classification [13]. Specifically, Deep Learning (DL) algorithms—a branch of machine learning, which uses architectures that possess many layers of processing [14]—have been massively used to detect CXRs [15] and CT scans [16,17] of infected lungs. In particular, Deep Neural Networks (DNNs) have been widely employed for this purpose [18,19].

Although DNNs have been applied with great success to identifying cases of the NCP [3,15–17,20,21], they still present some challenging limitations. First of all, DL architectures have a very large number of free parameters that must be adapted by the optimization algorithms. This means that, in order to achieve the convergence towards a robust solution, it is necessary to have a large amount of training data, which is not always possible in practice [14]. In addition, it is not certain that having lots of scans available is enough to be of quality [22]. This situation is further worsened by the fact that, since the COVID-19 is a relatively recent disease, the proportion of CXRs and CT scans related to NCP is very limited with respect to the number of images available in the datasets, freely available on the web [4]. Since most of the proposed DL approaches are of supervised type, an imbalance between the number of images in the training sets could provide poor results. In addition, the number of free parameters that must be adapted during the training leads to a high computational cost and many of the proposed DNN architectures can be trained only on powerful computers equipped with many GPUs in several hours.

Moreover, the identification of scans of patients infected by COVID-19 is a problem more similar to the anomaly detection rather than the traditional classification, due to the small number of data present in each dataset [23]. It would, therefore, be appealing to design an anomaly detection algorithm, which is light from the computational point of view, and is capable of identifying radiology scans related to COVID-19 with high accuracy. In this direction, some works have focused on the application of GAN-based approaches to detect anomalies in medical images [24,25]. However, such approaches suffer a not negligible computational cost.

Considering all the above challenging limitations in employing DL techniques for detecting scans of infected patients, we wonder whether DNNs are absolutely necessary to detect such scans, or simpler methodologies may instead perform in the same way as the DNNs, although they do not have, in general, advantages over DNNs.

Motivated by this still unanswered question, in this paper, we investigate whether traditional image processing techniques [26] can be reliable enough to detect images related to patients infected by COVID-19. Towards this end, we propose a histogram-based approach that exploits a suitable inter-histogram distance [27,28]: the histograms of some target images (belonging to a reference class, i.e., not images of infected lungs) are averaged

to produce a target histogram. This histogram is then used as a reference in the inference phase: for each unknown test scan, the related test histogram is obtained, and a suitable measurement of the distance between the tested and target histograms is evaluated. If this distance is below a certain threshold, the test image is classified the same as the target class; otherwise, it is considered an anomaly and labeled as COVID-19.

Overall, the main contributions of this paper may be so summarized:

- We propose a histogram-based technique to automatically detect the COVID-19 disease from CXRs and CT images. The histogram evaluation is a simple and very fast operation. In addition, in order to construct a target histogram, very few images are needed, in contrast to DNNs that have to use a huge number of scans to be trained.
- We investigate different inter-histogram distances to evaluate how an unknown scan is far from the target one. These distances are used to label the test images as normal (reference class) or anomaly (NCP), depending on whether they are less or greater than suitably set thresholds. Although all the proposed distances can be computed with the same computational cost, we expect that some of them work better in practice.
- We evaluate numerical results on benchmark datasets available in the open literature on CXRs and CT scans and compare the proposed approach to other state-of-the-art DNN-based architectures. We observed that the proposed approach, although very simple to implement, is able to obtain excellent results.

We expect that the main insight, deduced from the numerical results of the proposed approach, is that, at least when the images of the considered datasets are homogeneous enough (i.e., a few outliers are present), it is not really needed to resort to complex-to-implement DNNs, in order to attain an effective detection of the COVID-19 disease.

The rest of the paper is organized as follows. Section 2 presents the recent literature on the topic. Section 3 describes the proposed approach in terms of both the used methodology and inter-histogram distances, as well as introduces the experimental setup. Section 4 presents the obtained numerical results and performance comparisons, as well as provides the discussion on the proposed idea. Finally, Section 5 concludes the paper and outlines some future research.

2. Related Work

During the last two decades, great attention of researchers has been focused on automatic classification of medical images, and, to that end, a plethora of different techniques have been employed [29]. Although some interpretations are still made by a visual inspection of the obtained scans, Computer-Aided Detection or Computer-Aided Diagnosis (CAD) facilities help radiologists to detect lesions on chest X-rays [29]. However, in its early stage of usage, CAD can be defined solely as a computer analysis tool for image data. Over time, research efforts transformed CAD into automatic diagnostic tools [30].

The majority of the proposed approaches in the literature, principally devoted to the diagnosis of lung cancer [31], exploits low-level handcrafted features [32]. These approaches are founded on: texture-based features [33], edge-based features [34,35], graph mining [36], and color-based features [37–39]. Specifically, these works exploit different methodologies to perform image segmentation in regions of interest for building up masking operations that label them as either infected or not infected lungs.

In particular, such as the proposed approach, the works in Reference [40–42] exploit histogram-based information to characterize and/or classify medical images. In the past, histograms, due to the simplicity of their computation and accuracy of the produced results, have been widely used for object recognition [43–46], identification [47], and/or mining from images [27,28]. Among the applications in medical images, Ref. [41,42] used distance-based approach in detecting anomalies in images. Specifically, Reference [41] evaluates the histogram of a 3D volume of neuronal cells and fit them with a Gaussian function, in order to define different clusters in the images. Similar to the approach proposed in this paper, Reference [42] performs automatic segmentation of cell nuclei by exploiting an adaptive (local) threshold computed on the basis of the mean and standard deviation of the pixel

gray-level values. However, unlike the proposed approach, these works do not directly employ histograms to detect images of infected patients.

Many works have been focused on important classes of medical images, i.e., CXRs and CT scans. These studies analyze such images to detect tuberculosis [48–50] and lung cancer [51–54]. However, CXRs and CT scans can be useful also to detect other important diseases, such as viral or bacterial pneumonia [55,56].

In this regard, CXRs and CT scans have been massively used for the detection of COVID-19 disease. Although the pandemic is quite recent, several contributions are available in the literature. However, even if there are some sparse works about the manual screening of such images [57–61], almost all of the state-of-the-art approaches relate to the use of Machine Learning (ML) [62] and Deep Learning (DL) [63,64] techniques. The ML, in fact, could become a helpful and potential powerful tool for large-scale COVID-19 screening [13,65], and the author in Reference [3] has recently hypothesized that DL techniques applied to CT scans can become the first alternative screening test to the rRT-PCR in the near future. Motivated by this expectation, in the last year, the DL has been successfully used for CXRs [15,20,66,67], CT scans [56,68–70], or both [18,71]. Being, indeed, challenging to summarize all the available literature in a single paper, there are some useful reviews regarding the application of DL techniques to COVID-19 detection on CXRs [72], CT scans [73,74], and both [65,75]. A systematic review on the detection of COVID-19 using chest radiographs and CT scans, highlighting strongness and weakness of several different approaches, can be found in Reference [76]. There are also some surveys of related datasets available [77,78].

An overview of these works points out that DL approaches, mainly based on the supervised paradigm, can be divided into two main families: those based on segmentation and those that perform the classification task directly. The approaches, which are based on segmentation, are usually founded on U-Net type architecture to identify relevant part of the CXRs/CT scans and perform classification, focusing the attention only on these sections [56,79–84]. The second family of approaches, instead, is based on the binary classification problem of COVID/Non-COVID images [20,69,70,85–88] and utilize deep Convolutional Neural Networks (CNNs) and their variants, including VGG16, InceptionV3, ResNet, and DenseNet.

Finally, we point out that there are a few approaches that exploit the unsupervised paradigm, such as the use of deep auto-encoders [89–92]. Specifically, these works rely on deep or stacked autoencoders to automatically extract a set of meaningful features and then use softmax classifiers on the top to distinguish images of infected lungs from the healthy ones.

Among DL approaches, there exist some papers that exploit image histograms [93–99]. Specifically, the work in Reference [93], after a pre-processing with a median filter, extracts meaningful features from cropped regions by using Histogram Orientation Gradients (HOGs) and uses a final classification stage with a feed-forward neural network. Reference [94] introduces a pre-processing step based on the Contrast Limited Adaptive Histogram Equalization (CLAHE) idea to improve the contrast and generate an enhanced CXR image. Authors in Reference [95] propose a statistical histogram-based method for the pre-categorization of skin lesion: the image histogram is used to check the image contrast variations and classify these images into high and low contrast images. Similarly, Reference [98] uses histogram thresholding techniques to perform image clustering and then propose an image segmentation method for skin lesion delineation. Authors in Reference [96] propose ImHistNet, a deep neural network for end-to-end texture-based image classification based on a variant of the learnable histogram introduced in Reference [100] for pattern detection in pictures. The work in Reference [97], similar to our approach, extracts features from suitable inter-histogram distances but uses these features by feeding them into several (supervised) classifiers. Similarly, Reference [99] uses histogram to extract meaningful features, along with other statistical characterizations, and then performs a final classification through an artificial neural network. Moreover, the works

in Reference [101,102] exploit histogram-based enhanced techniques and metaheuristic approaches in Magnetic Resonance Imaging (MRI). Specifically, Reference [101] introduces MedGA, an image enhancement method based on Genetic Algorithms (GAs) that improves the threshold selection for the segmentation of the region of interest. MedGA uses a pre-processing stage for the enhancement of MR images based on some nonlinear histogram equalization techniques. Similarly, the work in Reference [102] proposes a Particle Swarm Optimized (PSO) texture-based histogram equalization technique to enhance the contrast of MRI brain images and find an optimal threshold for the segmentation. The obtained results overcome those of standard histogram equalization and those presented in Reference [101]. Finally, also the recent work in Reference [103] exploits DL segmentation-based histogram and threshold analysis in chest CT scans for differentiating healthy lungs from the infected ones. Specifically, the proposed method automatically derives imaging biomarkers from chest CT images based on histogram and provides a Hounsfield unit (HU) threshold analysis to assess differences in those biomarkers between lung-healthy individuals and those affected by atypical pneumonia.

Overall, although these last papers exploit the histogram in their approaches, they are substantially different from our work, since they exploit the histogram for: (i) enhancing the image quality; (ii) adjusting the contrast; and (iii) extracting features to be used by a final classifier. Moreover, only a couple of these papers focus on COVID-19 disease. Our approach, on the other hand, directly uses the histogram information to measure the distance from a target histogram and then decides whether or not an unknown CXR or CT image is related to a patient who is infected with COVID-19. This makes our approach an unsupervised method, which exhibits very limited implementation complexity.

A synoptic overview of the related work is provided in Table 1, that summarizes the main approaches pursued by the referred papers.

Table 1. A synoptic view of the main related work.

Family	Approach	Work	Image Type
Manual screening	CAD	[57]	CT
		[58]	CT
		[59]	CT
		[60]	CT
		[61]	CXR
Hand-crafted features	Texture-based features	[33]	Cells
	Edge-based features	[34]	Histopathological
		[35]	Cytological
	Graph mining	[36]	Histopathological
	Color-based features	[37]	Cells
		[38]	Histopathological
		[39]	Histopathological
Deep learning	Review	[72]	CXR
		[73]	CT
		[74]	CT
		[75]	CXR + CT
		[65]	CXR + CT
		[76]	CXR + CT
		[77]	CXR + CT
		[78]	CXR + CT
	Segmentation	[79]	CXR
		[80]	CT
		[81]	CT
		[82]	CT
		[56]	CT
		[83]	CXR
		[84]	CXR

Table 1. *Cont.*

Family	Approach	Work	Image Type
	Classification	[70]	CT
		[69]	CT
		[85]	CT
		[86]	CT
		[87]	CXR
		[20]	CXR
		[88]	CXR
	Unsupervised	[89]	Histopathological
		[90]	CT
		[91]	CT
		[92]	CXR
Histogram	Histogram + DL	[93]	CXR
		[94]	CXR
		[95]	Skin
		[96]	CT
		[97]	MRI
		[98]	Skin
		[99]	Skin
		[101]	MRI
		[102]	MRI
		[103]	CT

3. Materials and Methods

3.1. Proposed Approach

The proposed approach is based on evaluating a suitable distance between the histogram of an unknown image and a target histogram, which is obtained by averaging a number of histograms belonging to a target class (i.e., common pneumonia or normal). Afterward, if this distance is greater than a threshold, then the unknown image is labeled as anomaly, i.e., it presents COVID-19 disease; otherwise, it is labeled as the target class.

3.1.1. The Evaluation of the Target Histogram

Let $\mathcal{X} = \{X_k\}_{k=1}^{N_T}$ be a set composed of N_T target images (i.e., belonging to normal or CP diagnostics). Since both CT and CXR scans are grayscale images, the k-th input data X_k is modeled as a matrix of dimension $M \times N$, representing the number of rows and columns, respectively. The pixels' intensity values have been normalized into the range $[0, 1]$.

For each of the N_T images, the related histogram h_k, with $k = 1, \ldots, N_T$, is computed for N_{bin} bins. In this paper, we choose the (normalized) histogram as a statistical representation of the target, principally due to its simplicity and efficiency in computation. A histogram is an estimate of the probability distribution obtained by partitioning the range of values into a sequence of N_{bin} equally-spaced intervals (called *bins*) and counting how many values fall into each interval. The histogram is then normalized so that its sum total equates to one.

The N_{bin} bins, used to build up the histogram, should be chosen by a trade-off between numerical stability of the distance measurements and its discriminating capability. Although this number turned out not to be critical for the performance of the proposed approach, we found that an optimized setting to guarantee non-empty bins is to use 50 bins, i.e., $N_{bin} = 50$.

The *target histogram* is, hence, evaluated as the average of h_k, computed for each image, over N_T histograms:

$$\overline{h} = \frac{1}{N_T} \sum_{k=1}^{N_T} h_k. \tag{1}$$

Alternatively, since the histogram evaluation is a nonlinear operation, we have also tested the average of all the N_T target images followed by the evaluation of the histogram. However, we expect that this procedure gives a rise to inadequate results, as detailed in Section 4.5.

In this phase, we also evaluate the distance between the just computed target histogram $\bar{h}$ and the histogram h_k of every single k-th reference scan, by using suitable probability dissimilarity measurements (introduced in the next subsection). Among these distances, we compute the mean d_m and standard deviation σ_d values, in order to set conveniently a suitable threshold TH used during the test phase to discriminate a reference scan from an anomaly. The idea is that the statistical distance from an anomalous scan should be greater than a reference one. Therefore, the threshold TH would be set equal to the mean distance d_m plus a term depending on its standard deviation. Mathematically, we set the threshold TH as follows:

$$TH = d_m + \eta\sigma_d, \tag{2}$$

where η is a suitable constant. In the case of CT scans, we set $\eta = 2$, while, for CXRs, $\eta = 1.4$ provides good results.

During the inference phase, the test histogram of an unknown image is evaluated. This test histogram will be then compared to the target one, according to the same distance measurement used previously. If the distance between the test and target histograms rises beyond the threshold TH, the underlying image will be marked as COVID (anomaly); otherwise, it will be marked as the reference one. The proposed idea is shown in Figure 1, which depicts both the evaluation phase of the target histogram, as well as the inference phase, where an unknown image goes through the deduction process.
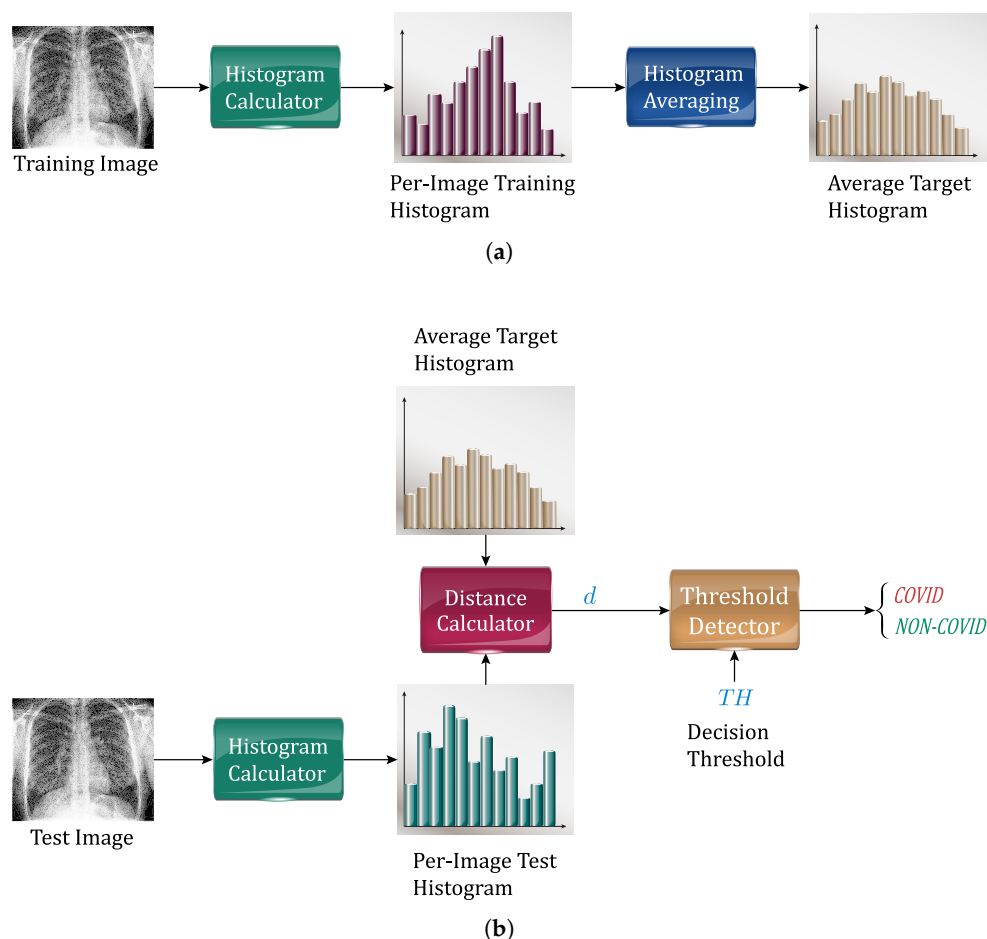

Figure 1. Proposed approach: (**a**) evaluation of the target histogram, and (**b**) inference phase for an unknown image.

3.1.2. The Considered Inter-Histogram Distances

Evaluation of the dissimilarity between the target histogram and that obtained from an unknown test image is a highly important issue.

In the literature, the similarity between the two histograms is evaluated by several distance measurements over the underlying distributions [104,105]. Regarding the aims of this paper, after denoting by p and q the two N_{bin}-dimensional vectors representing the involved histogram distributions, defined over the set of interval bins $\mathcal{I} = \{1, \ldots, N_{bin}\}$, we have selected the following four distances.

1. Cosine distance: It is formally defined as:

$$d_c = 1 - \frac{\sum_{i \in \mathcal{I}} p_i q_i}{\sqrt{\sum_{i \in \mathcal{I}} p_i^2} \sqrt{\sum_{i \in \mathcal{I}} q_i^2}}, \tag{3}$$

and it normally ranges in the interval $[0, 2]$. However, since we are considering probabilities, each bin value is non-negative (i.e., $p_i, q_i \geq 0$, for all i), so that the distance in (3) is limited to the interval $[0, 1]$. A distance equal to zero means that the two histogram are identical, while a distance equal to one denotes orthogonal histograms.

2. Kullback–Leibler (KL) divergence [106]: It is defined as:

$$d_{KL} = \sum_{i \in \mathcal{I}} p_i \log\left(\frac{p_i}{q_i}\right), \tag{4}$$

where p_i and q_i are the values of the p and q histogram in the i-th bin, respectively. By definition, the contribution of the i-th term in the summation in (4) is zero when p_i vanishes. It is always non-negative, and it is zero when the two distributions are equal.

3. Bhattacharyya distance [107]: It is defined as:

$$d_B = -\log\left(\sum_{i \in \mathcal{I}} \sqrt{p_i q_i}\right). \tag{5}$$

The Bhattacharyya distance, such as the KL divergence, is always non-negative, while it is vanishing when the two distributions are equal.

4. χ^2 distance: It is defined as:

$$d_{\chi^2} = \sum_{i \in \mathcal{I}} \frac{(p_i - q_i)^2}{p_i + q_i}. \tag{6}$$

In addition, the χ^2 distance is a non-negative measure.

These distances, except the cosine one, have been normalized by the number N_{bins} of used bins, in order to render them independent of the N_{bin} setting. The Bhattacharyya distance is widely used in several application, such as image processing, and, unlike the KL one, has the advantages of being insensitive to the zeros of distributions.

In the proposed approach, if the distance (chosen between the cosine, KL, Bhattacharyya, and χ^2 ones) between the target and a test histogram is above the set threshold TH of Equation (2), then, the image under test is classified as COVID-19 (CNP); otherwise, it is classified as the target class (normal or CP, depending on the used training set).

3.2. The Considered Datasets

In this work, we use two kinds of chest medical images: the chest CT scans and the traditional CXR images.

Regarding the CT scans, we have selected the COVIDx CT-2A dataset (It can be downloaded from: https://www.kaggle.com/hgunraj/covidxct (accessed on 20 May 2021), which has been constructed by collecting a number of open data sources [108,109] and comprises 194,922 CT slices from 3745 patients. The scans of the dataset are related to three classes: novel coronavirus pneumonia due to SARS-CoV-2 viral infection (NCP), common

pneumonia (CP), and normal (N) controls (i.e., images from non-infected individuals). For NCP and CP CT volumes, slices marked as containing lung abnormalities were leveraged. Moreover, all the CT volumes contain the background, in order to avoid model biases. An example of a representative image for each image class is reported in the first row of Figure 2.
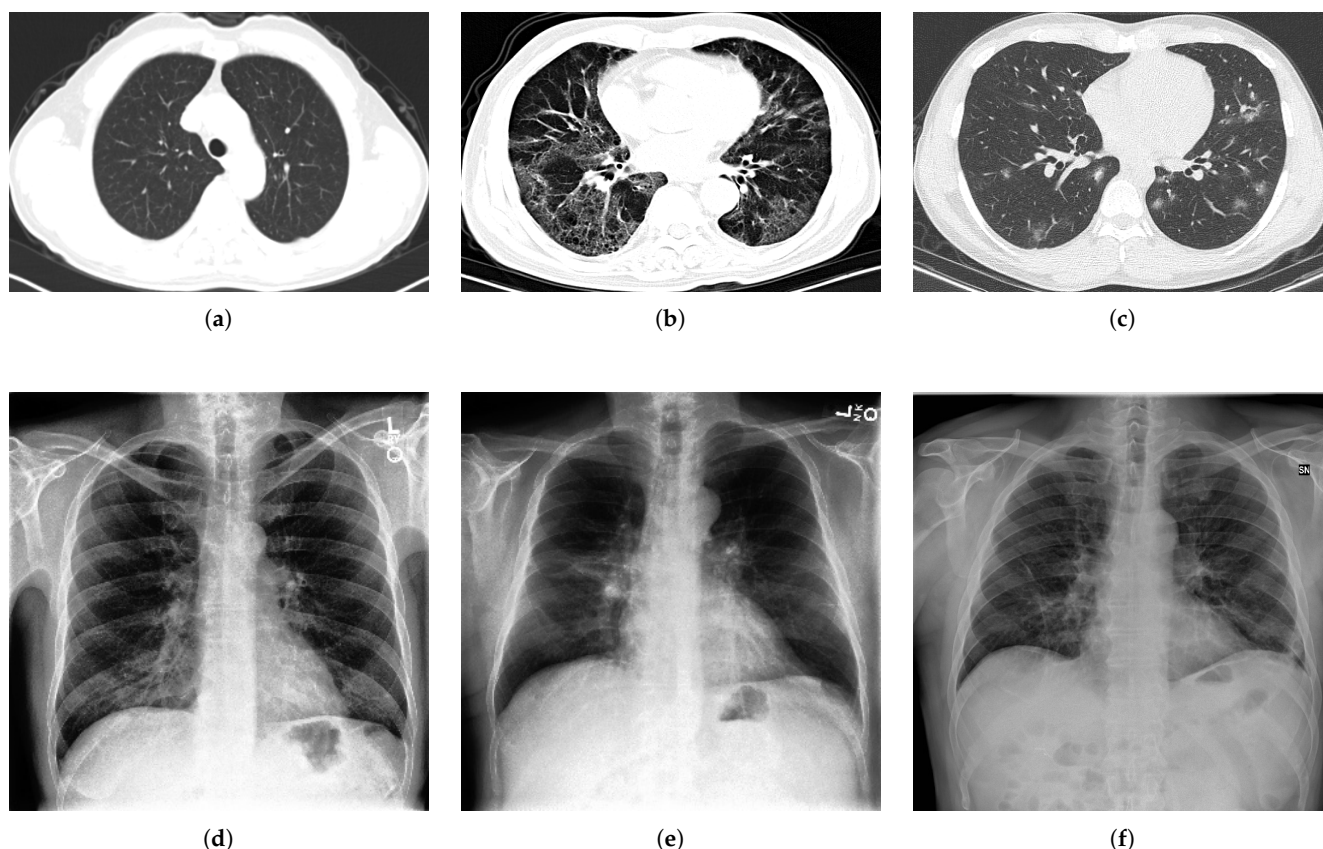

Figure 2. Examples of some chest CT and CXR images: (**a**) CT normal, (**b**) CT common pneumonia (CP), (**c**) CT novel coronavirus pneumonia (NCP), (**d**) RX normal, (**e**) RX CP, and (**f**) RX NCP.

In order to stress the effectiveness of the proposed approach in view of numerical comparisons, which are presented later, for the CXRs, we found a highly imbalanced dataset that contains few COVID images. This is a representative of the actual situation of public datasets, and it has been selected "ad hoc" to check the effectiveness of the proposed approach with respect to the corresponding supervised state-of-the-art approaches based on deep learning, which usually need a large amount of well-balanced training data.

Specifically, for the CXRs, we have selected the COVID-XRay-5K dataset (It can be downloaded form: https://github.com/shervinmin/DeepCovid (accessed on 20 May 2021), which has been constructed by collecting data from two publicly available sources [15]. The downloadable COVID-Xray-5k dataset is already split in training and test sets, and it contains 2084 training and 3100 test images. However, from the web URL, it can be downloaded a training set composed of only 580 Non-COVID and 84 COVID images, respectively, while the test set is composed of 3000 Non-COVID and 100 COVID images. An example of a representative image for each class is reported in the second row of Figure 2.

Since the COVID-19 disease causes a pneumonia, from both datasets, we have selected only pneumonia images as the Non-COVID target class. In addition, for validating the proposed approach, we also consider normal images as targets. Furthermore, from the CT dataset, we have randomly selected 3500 images for both the Pneumonia and COVID classes for evaluating the target and 500 images from both classes to test it. For the CXR

dataset, we used all the 580 images available for the Non-COVID class and the 84 images available for the COVID class to evaluate the target, while we selected 100 pneumonia images and all the available 97 COVID images for the test set. A summary of the used datasets is provided in Table 2. The same size of the target/test sets are used for the normal class. In the numerical results, we then select N_T target images from those available.

Table 2. Number of target and test images for each considered class and dataset.

	Computed Tomography		X-rays	
Type	**Target**	**Test**	**Target**	**Test**
COVID	3500	500	84	100
Non-COVID	3500	500	580	97

3.3. Built-Up Simulation Environment

All the carried out simulations have been implemented in Python environment by using the end-to-end and open-source deep learning platform TensorFlow 2 exploiting the Keras API. Simulations have been performed on a PC equipped with an Intel Core i7-4500U 2.4 GHz processor, 16 GB RAM, and Windows 10 operating system.

3.4. The Considered Performance Metrics

In a binary classification problem, we are interested in classifying items belonging to a *positive* class (P) versus a *negative* one (N). Therefore, there are four basic combinations of actual data category and assigned output category, namely:

- *True Positive* (TP): correct positive assignments;
- *True Negative* (TN): correct negative assignments;
- *False Positive* (FP): incorrect positive assignments; and
- *False Negative* (FN): incorrect negative assignments.

The set of these four metrics is usually arranged in a bi-dimensional matrix layout, called Confusion Matrix (CM), which allows a simple visualization of the performance of a binary classification algorithm. Specifically, each column of the CM represents the instances in a predicted class, while each row represents the instances in an actual class. Moreover, the combination of the previous four numbers in some powerful indicators can be a valid tool to quantitatively measure the performance of a classification algorithm [110]. Among all the possible combinations, in this paper, we focus on the accuracy, precision, recall, and F-measure metrics, whose formal definitions are briefly reported in Table 3. Accuracy is the ratio between the correct identified instances among their total number. Precision is the ratio of relevant instances among the retrieved instances, while the Recall is the ratio of the total amount of relevant instances that were actually retrieved. Finally, precision and recall can be combined in a single measurement, called F-measure, that is mathematically defined as their harmonic mean.

The state-of-the-art approaches have also been evaluated by the area under the Receiver Operating Characteristic (ROC) curve, abbreviated as AUC. The closer the AUC is to one, the better is the classifier performance. The ROC curve, which is a graphical representation of the performance of a binary classifier, is obtained by plotting the TP rate on the *y*-axis against the FP rate on the *x*-axis for increasing values of the decision threshold. The TP rate (formally coincident with the recall metric) and the FP rate are, respectively, the ratio of the number of TP to the total positive examples, and the ratio of the number of FP to the total negative examples, respectively. Their definition can be found in the last two rows of Table 3.

Table 3. The used performance metrics.

Performance Metrics	Formula
Precision	$TP/(TP + FP)$
Recall	$TP/(TP + FN)$
F-measure	$2TP/(2TP + FP + FN)$
Accuracy	$(TP + TN)/(TP + FN + FP + TN)$
TP rate	$TP/(TP + FN)$
FP rate	$FP/(FP + TN)$

4. Results and Discussion

In this section, we provide the numerical results, obtained from the proposed approach, on the two considered datasets. The performance has been evaluated by considering Non-COVID scans as the reference images to evaluate the target histograms. The Non-COVID class has been formed from images related to patients infected by common viral pneumonia (CP) or from healthy subjects (N). The performance comparisons with three state-of-the-art deep architectures are also presented. In the case of CT dataset, the test set, used in experiments, is composed of 500 CT scans belonging to the new coronavirus pneumonia (NCP) and 500 CT scans belonging to the reference class (CP or N). In the case of CXR dataset, instead, the test set, used in experiments, is composed of 100 CXRs belonging to the new coronavirus pneumonia (NCP) and 97 CXRs belonging to the reference class (CP or N). To provide a clear graphical representation of the obtained distances, the test instances have been fed into the proposed algorithm in this order: first, the NCP scans, and then the reference CP or N ones.

4.1. Evaluation of the Proposed Approach

In the first set of experiments, we investigate the choice of the inter-histogram distances of Section 3.1.2 on both datasets. In this experiment, we use the CP class as the reference. The results have been obtained by selecting $N_T = 500$ reference images and a number $N_{bin} = 50$ of histogram bins. Moreover, the η variable in (2) has been set to $\eta = 2$ for the CT dataset and to $\eta = 1.4$ for CXRs, respectively. Table 4 summarizes the results, obtained by the proposed approach, in terms of the Accuracy, Precision, Recall, and F-measure metrics, introduced in Section 3.4 and defined in Table 3.

The results of Table 4 support the effectiveness of the proposed approach. In fact, all of the considered metrics reach high values, and, interestingly enough, they reach the top result of 100% with some distance measurements. Table 4 also reports the mean d_m, standard deviation σ_d, and the related threshold TH obtained by Equation (2). The second column of this table shows that the actual value of σ_d depends on the selected inter-histogram distance. By a careful examination of the rows of Table 4, we can draw three main considerations:

- although all the considered distances provide good results for the CT datasets, the cosine distance is able to reach 100%;
- in case of CXR dataset, all the considered distances obtain the accuracy of 100%; and
- for both the datasets, the cosine distance provides the lower values of the standard deviation σ_d.

The results provided in Table 4 support the use of the cosine distance that works to advantage, compared to the other distance measurements. In fact, cosine distance is able to capture the "spatial" information provided by histograms, since it effectively measures their similarity, regardless of the single bin values. Motivated by these considerations, in the following tests and comparisons, we use the cosine distance.

Table 4. Results obtained by the proposed approach under the two considered datasets. The results have been obtained by using $N_T = 500$ reference images from the CP class and a number $N_{bin} = 50$ of histogram bins.

Model	d_m	σ_d	TH	Accuracy	Precision	Recall	F-Measure
Computed Tomography ($\eta = 2$)							
Proposed (Cosine)	0.0544	0.0664	0.1872	1.0000	1.0000	1.0000	1.0000
Proposed (KL)	0.1666	0.1218	0.4102	0.9870	0.9870	0.9870	0.9870
Proposed (Bhattacharyya)	0.0027	0.1037	0.2101	0.9870	0.9870	0.9870	0.9870
Proposed (χ^2)	0.2272	0.1119	0.4652	0.9860	0.9860	0.9860	0.9860
X-Rays ($\eta = 1.4$)							
Proposed (Cosine)	0.0339	0.0325	0.0794	1.0000	1.0000	1.0000	1.0000
Proposed (KL)	0.0011	0.0564	0.0801	0.9949	0.9950	0.9949	0.9949
Proposed (Bhattacharyya)	0.0027	0.0447	0.0653	1.0000	1.0000	1.0000	1.0000
Proposed (χ^2)	0.0016	0.0450	0.0645	1.0000	1.0000	1.0000	1.0000

In order to give visual insights about the results in Table 4 and justify the top 100% accuracy, we point out that Figure 3 shows the numerically evaluated spectra of the obtained cosine, KL, and Bhattacharyya distances. Since the χ^2 distance behaves as in the latter two distances, it is not explicitly depicted in the paper. This figure clearly shows the effectiveness of the proposed approach. In fact, we can see that the NCP CT scans (the first 500 bars in the left panels of Figure 3) are much more distant with respect to the corresponding reference images (the last 500 bars). Similar conclusions apply to the CXRs (the first 100 bars and last 97 bars in the right panels of Figure 3, respectively). The difference between the classes is about one order of magnitude for the cosine distance, while it is reduced for the KL divergence and the Bhattacharyya distance. These last cases also show a larger variance of the obtained distances with respect to the cosine distance, as already highlighted by the second column of Table 4. However, Figure 3 also underlines that the differences between the considered distances in the case of CXRs are more limited with respect to the CT case.

As a final consideration on these first results, both Table 4 and Figure 3 confirm that a lower value of the standard deviation σ_d makes the performance more robust with respect to the outliers eventually present in the tested dataset.

In order to validate the proposed approach, we repeat the first experiment by using the normal class (N), related to scans of healthy subjects, as reference. Results on both the datasets are shown in Table 5. This table shows that the results, obtained by using the normal class as the reference, provide metrics very similar to those shown in Table 4. Moreover, once again, by using the proposed cosine distance, all the considered performance metrics are unit-valued.
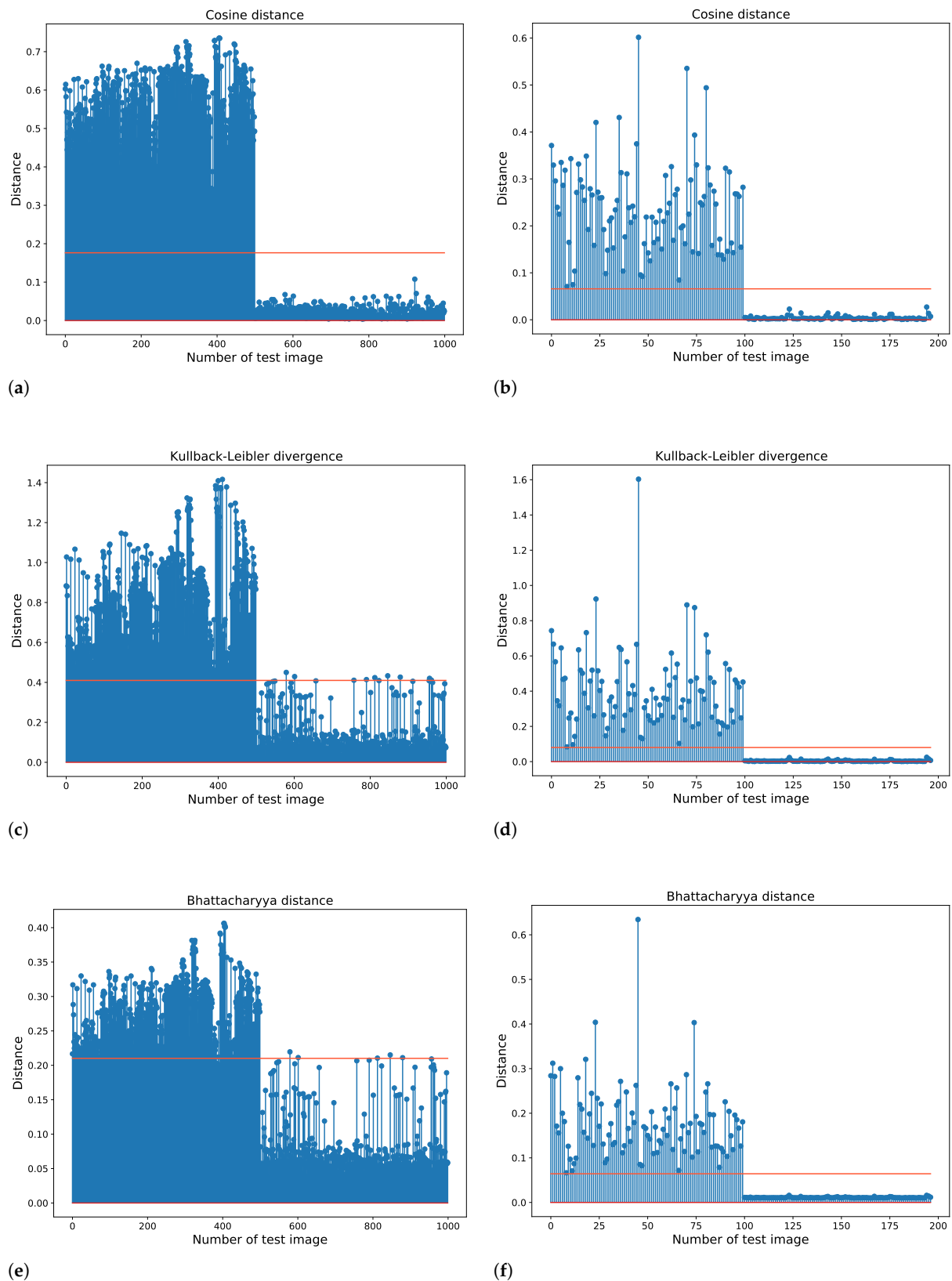
Figure 3. The obtained distances on the considered CT and CXRs datasets, and related threshold TH (the red lines) set using (2). The distances are: (**a**) Cosine for CT, (**b**) Cosine for CXRs, (**c**) Kullback–Leibler divergence for CT, (**d**) Kullback–Leibler divergence for CXRs, (**e**) Bhattacharyya distance for CT, and (**f**) Bhattacharyya distance for CXRs. The χ^2 distance behaves as in the KL and Bhattacharyya distances; hence, it is not explicitly shown. The results have been obtained by selecting $N_T = 500$ reference images and a number $N_{bin} = 50$ of histogram bins. The threshold in (2) has been set to $\eta = 2$ for the CT dataset and to $\eta = 1.4$ for CXRs.

Table 5. Results obtained by the proposed approach under the two considered datasets. The results have been obtained by using $N_T = 500$ reference images from the N class and a number $N_{bin} = 50$ of histogram bins.

Model	d_m	σ_d	TH	Accuracy	Precision	Recall	F-Measure
Computed Tomography ($\eta = 2$)							
Proposed (Cosine)	0.0458	0.0436	0.1330	1.0000	1.0000	1.0000	1.0000
Proposed (KL)	0.1231	0.1044	0.3319	0.9949	0.9950	0.9949	0.9949
Proposed (Bhattacharyya)	0.0048	0.0983	0.2014	0.9870	0.9870	0.9870	0.9870
Proposed (χ^2)	0.1783	0.0970	0.3723	0.9747	0.9748	0.9747	0.9747
X-Rays ($\eta = 1.4$)							
Proposed (Cosine)	0.0283	0.0292	0.0692	1.0000	1.0000	1.0000	1.0000
Proposed (KL)	0.0018	0.0509	0.0731	0.9898	0.9898	0.9898	0.9898
Proposed (Bhattacharyya)	0.0023	0.0415	0.0604	1.0000	1.0000	1.0000	1.0000
Proposed (χ^2)	0.0015	0.0398	0.0572	0.9870	0.9870	0.9870	0.9870

4.2. Sensitivity of the Proposed Approach to the Parameter Settings

The next test is concerned with the setting of the number N_{bin} of bins, used in the histogram evaluation. As already mentioned, the number of bins, used to construct the histogram should attain a suitable trade-off between numerical stability of the distance measurement and its discriminating capability. Table 6 summarizes the obtained results using the cosine distance in Equation (3). In this test, we again use $N_T = 500$ target images, while the constant η, in Equation (2), has been set to $\eta = 2$ for the CT dataset and to $\eta = 1.4$ for the CXRs, respectively.

Table 6. Results obtained by the proposed approach for different number N_{bin} of histogram bins. The reported performance metrics refer to the cosine distance at $N_T = 500$ reference images.

N_{bins}	d_m	σ_d	TH	Accuracy	Precision	Recall	F-Measure
Computed Tomography ($\eta = 2$)							
5	0.0222	0.0169	0.0560	0.7840	0.7927	0.7840	0.7824
10	0.0331	0.0258	0.0847	0.9570	0.9604	0.9570	0.9569
25	0.0453	0.0441	0.1335	0.9880	0.9883	0.9880	0.9880
50	0.0544	0.0664	0.1872	1.0000	1.0000	1.0000	1.0000
100	0.0558	0.0832	0.2222	1.0000	1.0000	1.0000	1.0000
250	0.0646	0.1225	0.3096	0.9960	0.9960	0.9960	0.9960
500	0.0764	0.1454	0.3672	0.9960	0.9960	0.9960	0.9960
X-Rays ($\eta = 1.4$)							
5	0.0005	0.0045	0.0068	0.9260	0.9261	0.9260	0.9260
10	0.0133	0.0143	0.0333	0.9880	0.9883	0.9880	0.9880
25	0.0236	0.0259	0.0598	1.0000	1.0000	1.0000	1.0000
50	0.0339	0.0325	0.0794	1.0000	1.0000	1.0000	1.0000
100	0.0076	0.0380	0.0608	1.0000	1.0000	1.0000	1.0000
250	0.0122	0.0430	0.0724	1.0000	1.0000	1.0000	1.0000
500	0.0135	0.0568	0.0931	0.9898	0.9898	0.9898	0.9898

Table 6 shows that the performance of the proposed approach is quite independent of the choice of the number N_{bins} of histogram bins for the CXR dataset, since it remains quite stable. However, its effect is more noticeable for the CT dataset. Although the standard deviation σ_d decreases with a smaller number of bins, the best performance in terms of all the considered metrics is obtained with a number of bins from 50 to 100 in the case of CT dataset. Hence, in order to obtain the best performance in both the datasets and maintain a limited computational complexity, we select $N_{bin} = 50$ definitively.

We also evaluate the robustness of the proposed approach with respect to the number N_T of target images. Towards this end, we evaluate the target histogram by averaging N_T histogram representations of the corresponding scans. Table 7 summarizes the obtained results using the cosine distance in (3). In this test, we again used $N_{bin} = 50$ histogram bins, while the threshold in (2) has been set to $\eta = 2$ for the CT dataset and to $\eta = 1.4$ for CXR one, respectively.

Table 7. Results obtained by the proposed approach at different number N_T of target images. The metrics have been evaluated by using the cosine distance and $N_{bin} = 50$ histogram bins.

N_T	d_m	σ_d	TH	Accuracy	Precision	Recall	F-Measure
Computed Tomography ($\eta = 2$)							
5	0.0351	0.0911	0.2173	0.8968	0.8968	0.8968	0.8968
10	0.0312	0.0911	0.2134	0.9880	0.9883	0.9880	0.9880
25	0.0383	0.0852	0.2087	0.9960	0.9960	0.9960	0.9960
50	0.0414	0.0787	0.1988	1.0000	1.0000	1.0000	1.0000
100	0.0460	0.0728	0.1916	1.0000	1.0000	1.0000	1.0000
250	0.0501	0.0704	0.1909	1.0000	1.0000	1.0000	1.0000
500	0.0544	0.0664	0.1872	1.0000	1.0000	1.0000	1.0000
3500	0.0732	0.0566	0.1864	1.0000	1.0000	1.0000	1.0000
X-Rays ($\eta = 1.4$)							
5	0.0022	0.0807	0.1152	0.7817	0.8474	0.7817	0.7700
10	0.0031	0.0724	0.1045	0.9188	0.9300	0.9188	0.9188
25	0.0076	0.0722	0.1087	0.9137	0.9262	0.9137	0.9129
50	0.0125	0.0669	0.1062	0.9645	0.9669	0.9645	0.9644
100	0.0179	0.0492	0.0868	0.9898	0.9901	0.9898	0.9898
250	0.0257	0.0329	0.0718	1.0000	1.0000	1.0000	1.0000
500	0.0339	0.0325	0.0794	1.0000	1.0000	1.0000	1.0000

Table 7 shows that, especially for the CT dataset, the performance of the proposed approach is quite insensible to the choice of the number N_T of target images in a large interval, since performance remains unchanged, even if the standard deviation tends to decrease by increasing the number of used images, because this depends on their average. However, we can see a gradual degradation in performance by reducing the number N_T of target images. On the basis of these results, we used 500 target images to maintain the standard deviation at an appropriate lower value.

The last test on the sensitivity of the proposed approach is concerned with the choice of the η parameter in Equation (2). To this end, we vary the η parameter inside the interval $[0, 5]$, with a step-size equal to 0.1, for a total of 51 different values, and we graphically report the corresponding obtained accuracy (measured in percentage). Figure 4 shows the results for both the considered datasets. These results have been evaluated by using the cosine distance, a number $N_T = 500$ of target images, and a number $N_{bin} = 50$ of histogram bins. Figure 4 clearly shows that there is a suitable range of η values that produces the accuracy of 100%, while the performance rapidly decreases with vanishing η (that means the threshold in Equation (2) is set on the basis of the mean distance d_m only) or with increasing η values. Figure 4 also shows that this range is independent of the used dataset, since its corresponding value for the CT is larger than that of the CXR dataset. However, the range producing the top accuracy is sufficiently wide to confirm the robustness of the proposed approach. In order to guarantee the broadest margin, we have set the η parameter at the value corresponding to approximately the middle of the range, i.e., $\eta = 2$ for CT dataset and $\eta = 1.4$ for CXR dataset.
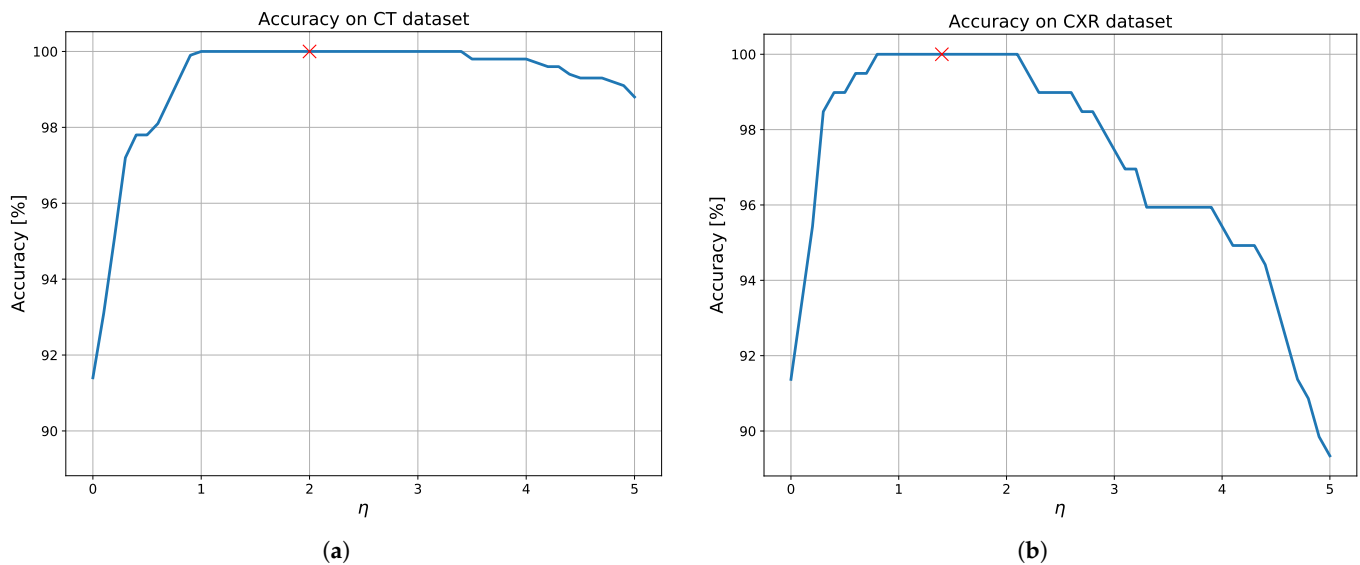
Figure 4. Accuracy (in %) as a function of the η parameter: (**a**) CT dataset and (**b**) CXR dataset. The best selected values ($\eta = 2$ for CT dataset and $\eta = 1.4$ for CXR dataset) are shown with a red cross. The results have been evaluated by using the cosine distance, a number $N_T = 500$ of target images, and a number $N_{bin} = 50$ of histogram bins.

4.3. Performance Comparison with an Alternative Histogram-Based Benchmark Approach

In order to numerically validate the chosen order of the mathematical operations to compute the target histogram shown in Figure 1, we test the proposed approach by considering an alternative method of evaluation. Different from the proposed methodology, shown in Figure 1, in the present experiment, we perform the average of all the $N_T = 500$ target images, and then we evaluate the corresponding histogram. This last idea is sketched in Figure 5 and could affect the performance, since the whole process is nonlinear. The inference phase remains unchanged with respect to our original idea. Once again, we use a number $N_{bin} = 50$ of histogram bins, and results are obtained with using the cosine distance in (3).
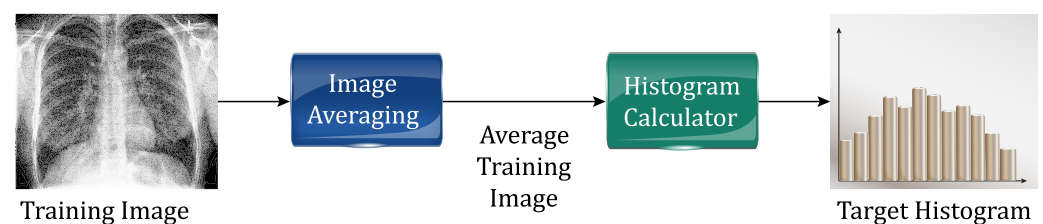

Figure 5. Target evaluation under the alternative histogram-based approach.

The numerical results, obtained by using such an idea, are provided in Table 8 for both the considered datasets. An examination of the rows of this table clearly demonstrates that this alternative does not perform very well, since all the reported metrics are poorer with respect to the excellent results of the proposed idea, shown in Figure 3. Hence, we chose to: (i) first, compute each single histogram; then, (ii) evaluate the target by averaging all of them, as shown in the top part of Figure 1.

Table 8. Numerical results obtained by using the target histogram evaluated as in Figure 5. The results have been obtained by using the cosine distance, $N_T = 500$ reference images, and a number $N_{bin} = 50$ of histogram bins.

Architecture	Accuracy	Precision	Recall	F-Measure
CT	0.5460	0.5902	0.5460	0.4826
CXR	0.9137	0.9266	0.9137	0.9137

4.4. Performance Comparisons with the State-of-the-Art DNN-Based Approaches

In this subsection, we show some comparisons with other state-of-the-art benchmark solutions. Specifically, in this paper, we consider some well-known feed-forward deep networks in the literature, i.e., the AlexNet [111], the GoogLeNet [112], and the ResNet18 [113]. In this regard, we note that AlexNet is composed of the cascade of five convolutional layers and three (dense) fully connected layers, while the GoogLeNet is more complicated, since it is much deeper and constructed by stacking three convolutional layers, nine *inception* modules, and two dense layers. An inception module is a particular layer obtained by concatenating several convolution operations with different filter sizes and a max pooling operation. Finally, ResNet18 is composed of 18 layers ending with a dense layer with a softmax activation. Different from the previous networks, the central part of the ResNet18 is a deep stack of residual units: these are composed of two convolutional layers (without pooling layer), with Batch Normalization and ReLU activation, using 3×3 kernels and preserving spatial dimensions.

Since these architectures are of supervised type, they have been trained by using both the CP and NCP classes in the training set. The training has been performed by using the Adam algorithm [114] with the default values ($\beta_1 = 0.9$, $\beta_2 = 0.999$, and $\varepsilon = 10^{-7}$), a batch size $N_b = 16$, and a learning rate set to $\mu = 10^{-6}$. The training has been executed for a total of 60 epochs.

The results, provided by these state-of-the-art supervised DNNs, are shown in Table 9.

Table 9. Performance of the tested benchmark DNNs. These architectures have been trained and tested on the whole datasets in Table 2.

Architecture	Accuracy	Precision	Recall	F-Measure	AUC
		Computed Tomography			
AlexNet	0.7110	0.8601	0.7110	0.7343	0.9460
GoogLeNet	1.0000	1.0000	1.0000	1.0000	1.0000
ResNet18	0.9130	0.9281	0.9130	0.9137	0.9130
		X-Rays			
AlexNet	0.9340	0.9341	0.9340	0.9340	0.9340
GoogLeNet	0.9746	0.9794	0.9694	0.9744	0.9750
ResNet18	0.9695	0.9697	0.9695	0.9695	0.9700

These results point out that AlexNet performs worse than our approach, since it reaches merely a degree of 71% and 93% accuracy for the CT and CXR, respectively, and, in addition, in terms of other performance metrics. The performance of GoogLeNet is the same as the proposed approach under the CT dataset but is worse than the one of the proposed approach under the CXR dataset. This lower performance in the case of CXR images is due to the limited number of training images used during the learning. However, we have to remark that the high performance of GoogLeNet on CT is obtained by a deep architecture that uses a huge number of free parameters compared to the proposed approach, as shown in Table 10, which reports, for completeness, the number of trainable parameters and the training time (in minutes) for all the considered architectures and

datasets. In our approach, we use only one free parameter, the adaptive threshold in Equation (2). Once again, this consideration, along with the trade-off shown in Table 10, supports the actual effectiveness of the proposed methodology.

Table 10. Computational complexity of the tested models ("M" stands for millions of parameters). The training time, in minutes, refers to data sets composed of images of size 300×200 pixels for the CT dataset and 320×390 pixels for the CXR dataset. The number of images is presented in Table 2.

Model	# param.	Training Time CT	Training Time CXRs
Proposed	1	0.31	0.087
AlexNet	58 M	223	62
GoogLeNet	6 M	258	73
ResNet18	11 M	290	84

4.5. Performance Robustness of the Considered Approaches

The aim of this last subsection is to evaluate the performance robustness of the proposed histogram-based approach, compared to the considered state-of-the-art DNN architectures.

In order to provide a visual interpretation of the results, shown in Table 9, and check how robust these solutions are regarding the testing images, Figure 6 shows, for both the considered datasets, the confusion matrices obtained by the state-of-the-art (supervised) DNNs.

The confusion matrices in Figure 6 clearly show the poor robustness of the DNN approaches. They illustrate that the main confusion is for the Non-COVID class, where, especially, in the case of CT scans, many instances are erroneously classified.

4.6. Limitations of the Proposed Approach

In this subsection, we outline some limitations of the proposed approach with respect to the DL-based ones.

We underline that the DNN methods can produce a spectrum of a posterior probabilities that may be, in turn, used as indexes of the reliability of the taken decision. This is possible only by the prior learning performed by such approaches. In our approach, instead, the reliability is directly measured by the value of the inter-histogram distance used in the discrimination phase. Although this distance may be used as (coarse) reliability index, nevertheless, it is not more informative than the corresponding spectrum of posterior probabilities nor is it related to the probability spectrum in a direct way.

As highlighted in previous numerical results, we have identified some datasets where the proposed approach is able to attain the unit-valued accuracy. However, the performance obtained on other datasets could be not so significant, since the effectiveness of the histogram comparison depends on the quality of the scanned images and the way used to be recorded. DNNs, due to their prior learning phase, are expected to be less sensitive, indeed, to the image characteristics.

To recap, DNN-based approaches are expected to be more flexible, powerful, and generalizable than the proposed approach, but at the cost of larger datasets, higher computational resources, and longer training time. After stressing this, we point out that the goal of this paper is not the introduction of a general methodology but, rather, showing that, under some operating conditions, a simple and computationally efficient approach can produce good results.
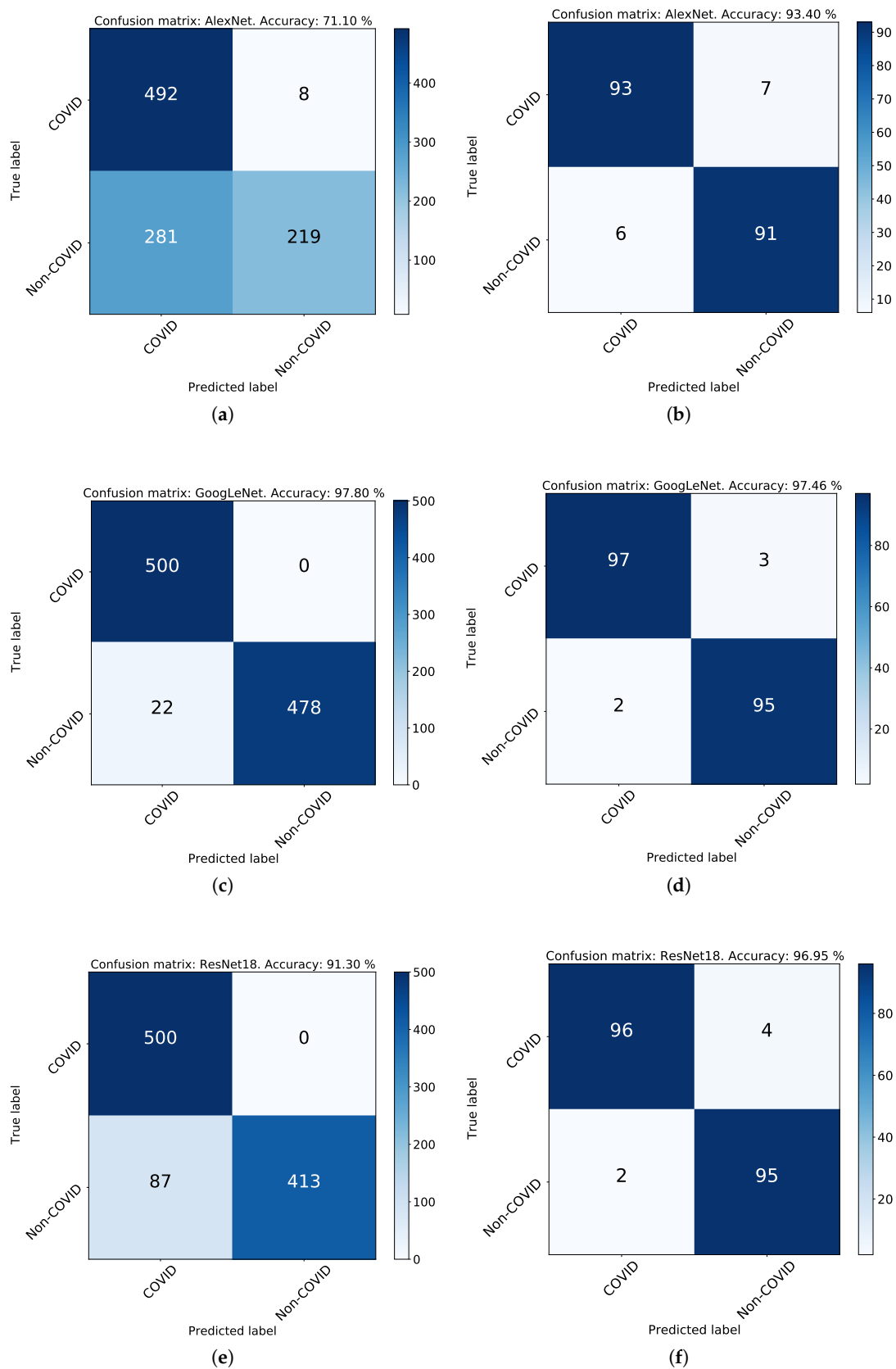
Figure 6. The confusion matrices obtained by the considered state-of-the-art supervised approaches: (**a**) AlexNet for CT, (**b**) AlexNet for CXRs, (**c**) GoogLeNet for CT, (**d**) GoogLeNet for CXRs, (**e**) ResNet18 for CT, and (**f**) ResNet18 for CXRs.

5. Conclusions and Hints for Future Research

In this paper, we investigate whether a traditional histogram-based approach can be used for the detection of CT and CXR scans of infected lungs. Specifically, we propose a histogram-based approach to detecting the new coronavirus pneumonia from CT and CXR scans. Since the number of these images is not high, we evaluate a target histogram on a reference class (i.e., normal or common pneumonia). A suitable inter-histogram distance is then used to evaluate how far this target histogram is from the corresponding histogram evaluated for an unknown test scan: if this distance is above a threshold, the test image is classified as anomaly, i.e., affected by the COVID-19 disease; otherwise, it is classified the same as the target class. A number of numerical results, evaluated on two open-source benchmark datasets, demonstrates the effectiveness of the proposed approach, since it is able to obtain a top degree of the considered performance metrics (i.e., accuracy, precision, recall, and F-measure), equal to unit value, comparable to the corresponding state-of-the-art DNN approaches, but with a limited computational complexity.

In a nutshell, the main lesson stemming from the reported performance comparisons is that, at least when the images, embraced by the considered datasets, are homogeneous enough (i.e., few outliers are present, so that the standard deviations σ_d of the corresponding inter-histogram (normalized) distances are limited up to 0.1), it is not really needed to resort to complex-to-implement DNNs, in order to attain reliable detection of the COVID-19 disease. The proposed histogram-based approach attains, indeed, very good detection performance, comparable with those of DNNs, but at an (extremely) reduced implementation complexity and training time (see Table 10).

In future works, we aim at extending our methodology to different types of medical images, other than CT, and/or different diseases. We expect, in fact, that the automatic screening by means of pathological images can take a great advantage by the simplicity of our methodology, in both the resulting accuracy and prediction time. To this end, it could be interesting to investigate, as a second line of research, more performing inter-histogram distances, such as the Earth Mover's Distance (EMD) [115], which measures how much work it would take to transform one histogram shape into another. A third hint of future research can be addressed towards the use of Varational Autoencoeders (VAEs) and Generative Adversarial Networks (GANs) for generating additional examples in the case of new variants of COVID-19, in order to be fast in the automatic discrimination of these scans without awaiting the construction of sufficiently copious dataset. Finally, a fourth line of future research can be focused on the implementation of the proposed methodology atop distributed Cloud/Fog Computing technological platforms [116,117], in order to produce fast and reliable clinical responses by exploiting the low-delay (and, possibly, multi-antenna empowered [118,119]) capability of the supporting broadband wireless access networks [120].

Author Contributions: Conceptualization, M.S. and E.B.; methodology, M.S., E.B. and L.P.; software, M.S. and S.S.A.; validation, A.M., M.S., L.P. and S.S.A.; formal analysis, E.B. and M.S.; investigation, M.S., L.P. and E.B.; data curation, A.M. and S.S.A.; writing—original draft preparation, M.S.; writing—review and editing, M.S., L.P. and A.M.; visualization, A.M.; supervision, E.B.; funding acquisition, E.B. All authors have read and agreed to the published version of the manuscript.

Institutional Review Board Statement: Not applicable.

Informed Consent Statement: Not applicable.

Data Availability Statement: Publicly available datasets were analyzed in this study. CT data can be found here: https://www.kaggle.com/hgunraj/covidxct (accessed on 20 May 2021), while CXR data can be found here: https://github.com/shervinmin/DeepCovid (accessed on 20 May 2021).

Conflicts of Interest: The authors declare no conflict of interest.

Abbreviations

The following main abbreviations are used in this paper:

AI	Artificial Intelligence
AUC	Area Under the Curve
CAD	Computer-Aided Diagnosis
CNN	Convolutional Neural Network
CM	Confusion Matrix
CP	Common Pneumonia
CT	Computed Tomography
CXR	Chest X-ray
DL	Deep Learning
DNN	Deep Neural Network
FN	False Negative
FP	False Positive
HOG	Histogram Orientation Gradients
KL	Kullback–Leibler
ML	Machine Learning
MRI	Magnetic Resonance Imaging
NCP	Novel COVID-19 Pneumonia
ROC	Receiver Operating Characteristic
TN	True Negative
TP	True Positive

References

1. Dhama, K.; Khan, S.; Tiwari, R.; Sircar, S.; Bhat, S.; Malik, Y.S.; Singh, K.P.; Chaicumpa, W.; Bonilla-Aldana, D.K.; Rodriguez-Morales, A.J. Coronavirus Disease 2019—COVID-19. *Clin. Microbiol. Rev.* **2020**, *33*, 1–48. [CrossRef] [PubMed]
2. Zhang, H.; Du, F.; Cao, X.J.; Feng, X.I.; Zhang, H.P.; Wu, Z.X.; Wang, B.F.; Zhang, H.J.; Liu, R.; Yang, J.J.; et al. Clinical characteristics of coronavirus disease 2019 (COVID-19) in patients out of Wuhan from China: A case control study. *BMC Infect. Dis.* **2021**, *21*, 207. [CrossRef]
3. Sharma, S. Drawing insights from COVID-19-infected patients using CT scan images and machine learning techniques: A study on 200 patients. *Environ. Sci. Pollut. Res.* **2020**, *27*, 37155–37163. [CrossRef]
4. Chen, S.G.; Chen, J.Y.; Yang, Y.P.; Chien, C.S.; Wang, M.L.; Lin, L.T. Use of radiographic features in COVID-19 diagnosis: Challenges and perspectives. *J. Chin. Med. Assoc.* **2020**, *83*, 644–647. [CrossRef] [PubMed]
5. Fang, Y.; Zhang, H.; Xie, J.; Lin, M.; Ying, L.; Pang, P.; Ji, W. Sensitivity of Chest CT for COVID-19: Comparison to RT-PCR. *Radiology* **2020**, *296*, E115–E117. [CrossRef]
6. Suetens, P. *Fundamentals of Medical Imaging*, 2nd ed.; Cambridge University Press: Cambridge, UK, 2009.
7. Hsieh, J. *Computed Tomography: Principles, Design, Artifacts, and Recent Advances*, 2nd ed.; John Wiley & Sons: Hoboken, NJ, USA, 2009.
8. Kanne, J.P.; Little, B.P.; Chung, J.H.; Elicker, B.M.; Ketai, L.H. Essentials for Radiologists on COVID-19: An Update—Radiology Scientific Expert Panel. *Radiology* **2020**, *296*, E113–E114. [CrossRef] [PubMed]
9. Rousan, L.A.; Elobeid, E.; Karrar, M.; Khader, Y. Chest x-ray findings and temporal lung changes in patients with COVID-19 pneumonia. *BMC Pulm. Med.* **2020**, *20*, 245. [CrossRef]
10. Li, Y.; Xia, L. Coronavirus Disease 2019 (COVID-19): Role of Chest CT in Diagnosis and Management. *Am. J. Roentgenol.* **2020**, *214*, 1280–1286. [CrossRef]
11. Nishio, M.; Noguchi, S.; Matsuo, H.; Murakami, T. Automatic classification between COVID-19 pneumonia, non-COVID-19 pneumonia, and the healthy on chest X-ray image: Combination of data augmentation methods. *Sci. Rep.* **2020**, *10*, 17532. [CrossRef]
12. Al-Ameen, Z.; Sulong, G. Prevalent Degradations and Processing Challenges of Computed Tomography Medical Images: A Compendious Analysis. *Int. J. Grid Distrib. Comput.* **2016**, *9*, 107–118. [CrossRef]
13. Chowdhury, M.E.H.; Rahman, T.; Khandakar, A.; Mazhar, R.; Kadir, M.A.; Mahbub, Z.B.; Islam, K.R.; Khan, M.S.; Iqbal, A.; Al Emadi, N.; et al. Can AI Help in Screening Viral and COVID-19 Pneumonia? *IEEE Access* **2020**, *8*, 132665. [CrossRef]
14. Goodfellow, I.; Bengio, Y.; Courville, A. *Deep Learning*; MIT Press: Cambridge, MA, USA, 2016.

15. Minaee, S.; Kafieh, R.; Sonka, M.; Yazdani, S.; Soufi, G.J. Deep-COVID: Predicting COVID-19 from chest X-ray images using deep transfer learning. *Med. Image Anal.* **2020**, *65*, 101794. [CrossRef] [PubMed]
16. Shen, D.; Wu, G.; Suk, H. Deep Learning in Medical Image Analysis. *Annu. Rev. Biomed. Eng.* **2017**, *19*, 221–248. [CrossRef]
17. Zhou, S.K.; Greenspan, H.; Shen, D. (Eds.) *Deep Learning for Medical Image Analysis*; Academic Press: Cambridge, MA, USA, 2017.
18. Mukherjee, H.; Ghosh, S.; Dhar, A.; Obaidullah, S.; Santosh, K.C.; Roy, K. Deep neural network to detect COVID-19: One architecture for both CT Scans and Chest X-rays. *Appl. Intell.* **2021**, *51*, 2777–2789. [CrossRef]
19. Sarv Ahrabi, S.; Scarpiniti, M.; Baccarelli, E.; Momenzadeh, A. An Accuracy vs. Complexity Comparison of Deep Learning Architectures for the Detection of COVID-19 Disease. *Computation* **2021**, *9*, 3. [CrossRef]
20. Madaan, V.; Roy, A.; Gupta, C.; Agrawal, P.; Sharma, A.; Bologa, C.; Prodan, R. XCOVNet: Chest X-ray Image Classification for COVID-19 Early Detection Using Convolutional Neural Networks. *New Gener. Comput.* **2021**. [CrossRef]
21. Pham, T.D. Classification of COVID-19 chest X-rays with deep learning: New models or fine tuning? *Health Inf. Sci. Syst.* **2021**, *9*, 2. [CrossRef]
22. Aiello, M.; Cavaliere, C.; D'Albore, A.; Salvatore, M. The Challenges of Diagnostic Imaging in the Era of Big Data. *J. Clin. Med.* **2019**, *8*, 316. [CrossRef] [PubMed]
23. Chandola, V.; Banerjee, A.; Kumar, V. Anomaly detection: A survey. *ACM Comput. Surv.* **2009**, *41*, 15. [CrossRef]
24. Han, C.; Rundo, L.; Murao, K.; Noguchi, T.; Shimahara, Y.; Milacski, Z.A.; Koshino, S.; Sala, E.; Nakayama, H.; Satoh, S.I. MADGAN: Unsupervised medical anomaly detection GAN using multiple adjacent brain MRI slice reconstruction. *BMC Bioinform.* **2021**, *22*, 31. [CrossRef]
25. Nakao, T.; Hanaoka, S.; Nomura, Y.; Murata, M.; Takenaga, T.; Miki, S.; Watadami, T.; Yoshikawa, T.; Hayashi, N.; Abe, O. Unsupervised Deep Anomaly Detection in Chest Radiographs. *J. Digit. Imaging* **2021**, *34*, 418–427. [CrossRef] [PubMed]
26. Solomon, C.; Breckon, T. *Fundamentals of Digital Image Processing: A Practical Approach with Examples in Matlab*; John Wiley & Sons: Hoboken, NJ, USA, 2011.
27. Brunelli, R.; Mich, O. Histograms analysis for image retrieval. *Pattern Recognit.* **2001**, *34*, 1625–1637. [CrossRef]
28. Conci, A.; Castro, E.M.M.M. Image mining by content. *Expert Syst. Appl.* **2002**, *23*, 377–383. [CrossRef]
29. Giger, M.L.; Chan, H.; Boone, J. Anniversary Paper: History and status of CAD and quantitative image analysis: The role of Medical Physics and AAPM. *Med. Phys.* **2008**, *35*, 5799–5820. [CrossRef]
30. Ranschaert, E.R.; Morozov, S.; Algra, P.R. (Eds.) *Artificial Intelligence in Medical Imaging—Opportunities, Applications and Risks*; Springer: Cham, Switzerland, 2019. [CrossRef]
31. Doi, K. Computer-aided diagnosis in medical imaging: Historical review, current status and future potential. *Comput. Med. Imaging Graph.* **2007**, *31*, 198–211. [CrossRef]
32. Irshad, H.; Veillard, A.; Roux, L.; Racoceanu, D. Methods for Nuclei Detection, Segmentation, and Classification in Digital Histopathology: A Review—Current Status and Future Potential. *IEEE Rev. Biomed. Eng.* **2014**, *7*, 97–114. [CrossRef] [PubMed]
33. Liu, T.; Li, G.; Nie, J.; Tarokh, A.; Zhou, X.; Guo, L.; Malicki, J.; Xia, W.; Wong, S.T.C. An Automated Method for Cell Detection in Zebrafish. *Neuroinformatics* **2008**, *6*, 5–21. [CrossRef] [PubMed]
34. Ali, S.; Madabhushi, A. An Integrated Region-, Boundary-, Shape-Based Active Contour for Multiple Object Overlap Resolution in Histological Imagery. *IEEE Trans. Med. Imaging* **2012**, *31*, 1448–1460. [CrossRef]
35. Filipczuk, P.; Fevens, T.; Krzyżak, A.; Monczak, R. Computer-Aided Breast Cancer Diagnosis Based on the Analysis of Cytological Images of Fine Needle Biopsies. *IEEE Trans. Med. Imaging* **2013**, *32*, 2169–2178. [CrossRef]
36. Bernardis, E.; Yu, S.X. Pop out many small structures from a very large microscopic image. *Med. Image Anal.* **2011**, *15*, 690–707. [CrossRef]
37. Schmitt, O.; Hasse, M. Radial symmetries based decomposition of cell clusters in binary and gray level images. *Pattern Recognit.* **2008**, *41*, 1905–1923. [CrossRef]
38. Wang, H.; Xing, F.; Su, H.; Stromberg, A.; Yang, L. Novel image markers for non-small cell lung cancer classification and survival prediction. *BMC Bioinform.* **2014**, *15*, 310. [CrossRef] [PubMed]
39. Al-Kofahi, Y.; Lassoued, W.; Lee, W.; Roysam, B. Improved Automatic Detection and Segmentation of Cell Nuclei in Histopathology Images. *IEEE Trans. Biomed. Eng.* **2010**, *57*, 841–852. [CrossRef]
40. Linguraru, M.G.; Wang, S.; Shah, F.; Gautam, R.; Peterson, J.; Linehan, W.; Summers, R.M. Computer-Aided Renal Cancer Quantification and Classification from Contrast-enhanced CT via Histograms of Curvature-Related Features. In Proceedings of the Conference Proceedings—IEEE Engineering in Medicine and Biology Society, Minneapolis, MN, USA, 3–6 September 2009; pp. 6679–6682. [CrossRef]
41. Oberlaender, M.; Dercksen, V.J.; Egger, R.; Gensel, M.; Sakmann, B.; Hege, H.C. Automated three-dimensional detection and counting of neuron somata. *J. Neurosci. Methods* **2009**, *180*, 147–160. [CrossRef] [PubMed]
42. Nielsen, B.; Albregtsen, F.; Danielsen, H.E. Automatic segmentation of cell nuclei in Feulgen-stained histological sections of prostate cancer and quantitative evaluation of segmentation results. *Cytom. Part A* **2012**, *81*, 588–601. [CrossRef]
43. Freeman, W.T.; Roth, M. Orientation histograms for hand gesture recognition. In Proceedings of the International Workshop on Automatic Face and Gesture Recognition, Zurich, Switzerland, 2–4 June 1995; pp. 296–301.
44. Dalal, N.; Triggs, B. Histograms of oriented gradients for human detection. In Proceedings of the 2005 IEEE Computer Society Conference on Computer Vision and Pattern Recognition (CVPR'05), San Diego, CA, USA, 20–25 June 2005. [CrossRef]

45. Chatzichristofis, S.A.; Boutalis, Y.S. FCTH: Fuzzy color and texture histogram – A low level feature for accurate image retrieval. In Proceedings of the Ninth International Workshop on Image Analysis for Multimedia Interactive Services, Klagenfurt, Austria, 7–9 May 2008. [CrossRef]

46. Voravuthikunchai, W.; Crémilleux, B.; Jurie, F. Histograms of Pattern Sets for Image Classification and Object Recognition. In Proceedings of the IEEE Conference on Computer Vision and Pattern Recognition, Columbus, OH, USA, 23–28 June 2014; pp. 224–231. [CrossRef]

47. Rachmawati, E.; Khodra, M.L.; Supriana, I. Histogram based Color Pattern Identification of Multiclass Fruit using Feature Selection. In Proceedings of the 5th International Conference on Electrical Engineering and Informatics (ICEEI 2015), Denpasar, Indonesia, 10–11 August 2015. [CrossRef]

48. Melendez, J.; van Ginneken, B.; Maduskar, P.; Philipsen, R.H.H.M.; Reither, K.; Breuninger, M.; Adetifa, I.M.O.; Maane, R.; Ayles, H.; Sánchez, C.I. A Novel Multiple-Instance Learning-Based Approach to Computer-Aided Detection of Tuberculosis on Chest X-Rays. *IEEE Trans. Med. Imaging* **2014**, *34*, 179–192. [CrossRef] [PubMed]

49. Jaeger, S.; Karargyris, A.; Candemir, S.; Folio, L.; Siegelman, J.; Callaghan, F.; Xue, Z.; Palaniappan, K.; Singh, R.K.; Antani, S.; et al. Automatic tuberculosis screening using chest radiographs. *IEEE Trans. Med. Imaging* **2014**, *33*, 233–245. [CrossRef] [PubMed]

50. Song, D.J.; Tong, J.L.; Peng, J.C.; Cai, C.W.; Xu, X.T.; Zhu, M.M.; Ran, Z.H.; Zheng, Q. Tuberculosis screening using IGRA and chest computed tomography in patients with inflammatory bowel disease: A retrospective study. *J. Dig. Dis.* **2017**, *18*, 23–30. [CrossRef]

51. Caroline, C. Lung Cancer Screening with Low Dose CT. *Radiol. Clin. N. Am.* **2014**, *52*, 27–46. [CrossRef]

52. Shen, W.; Zhou, M.; Yang, F.; Yu, D.; Dong, D.; Yang, C.; Zang, Y.; Tian, J. Multi-crop Convolutional Neural Networks for lung nodule malignancy suspiciousness classification. *Pattern Recognit.* **2017**, *61*, 663–673. [CrossRef]

53. Bradley, S.; Bradley, S.; Abraham, S.; Grice, A.; Lopez, R.R.; Wright, J.; Farragher, T.; Shinkins, B.; Neal, R.D. Sensitivity of chest X-ray for lung cancer: Systematic review. *Br. J. Gen. Pract.* **2018**, *68*, 827–835. [CrossRef]

54. van Beek, E.J.; Mirsadraee, S.; Murchison, J.T. Lung cancer screening: Computed tomography or chest radiographs? *World J. Radiol.* **2015**, *7*, 189–193. [CrossRef]

55. Jain, R.; Nagrath, P.; Kataria, G.; Kaushik, V.S.; Hemanth, D.J. Pneumonia detection in chest X-ray images using convolutional neural networks and transfer learning. *Measurement* **2020**, *165*, 108046. [CrossRef]

56. Oulefki, A.; Agaian, S.; Trongtirakul, T.; Laouard, A.K. Automatic COVID-19 lung infected region segmentation and measurement using CT-scans images. *Pattern Recognit.* **2021**, *114*, 107747. [CrossRef]

57. Yang, R.; Li, X.; Liu, H.; Zhen, Y.; Zhang, X.; Xiong, Q.; Luo, Y.; Gao, C.; Zeng, W. Chest CT severity score: An imaging tool for assessing severe COVID-19. *Radiol. Cardiothorac. Imaging* **2020**, *2*, e200047. [CrossRef] [PubMed]

58. Sen, S.; Saha, S.; Chatterjee, S.; Mirjalili, S.; Sarkar, R. A bi-stage feature selection approach for COVID-19 prediction using chest CT images. *Appl. Intell.* **2021**. [CrossRef]

59. Li, K.; Fang, Y.; Li, W.; Pan, C.; Qin, P.; Zhong, Y.; Liu, X.; Huang, M.; Liao, Y.; Li, S. CT image visual quantitative evaluation and clinical classification of coronavirus disease (COVID-19). *Eur. Radiol.* **2020**, *30*, 4407–4416. [CrossRef] [PubMed]

60. Matos, J.; Paparo, F.; Mussetto, I.; Bacigalupo, L.; Veneziano, A.; Perugin Bernardi, S.; Biscaldi, E.; Melani, E.; Antonucci, G.; Cremonesi, P.; et al. Evaluation of novel coronavirus disease (COVID-19) using quantitative lung CT and clinical data: Prediction of short-term outcome. *Eur. Radiol. Exp.* **2020**, *4*, 39. [CrossRef] [PubMed]

61. Chamorro, E.M.; Tascón, A.D.; Sanz, L.I.; Vélez, S.O.; Borruel, S. Radiologic diagnosis of patients with COVID-19. *Radiología (Engl. Ed.)* **2021**, *63*, 56–73. [CrossRef]

62. de Bruijne, M. Machine learning approaches in medical image analysis: From detection to diagnosis. *Med. Image Anal.* **2016**, *33*, 94–97. [CrossRef]

63. Altaf, F.; Islam, S.M.S.; Akhtar, N.; Janjua, N.K. Going Deep in Medical Image Analysis: Concepts, Methods, Challenges, and Future Directions. *IEEE Access* **2019**, *7*, 99540–99572. [CrossRef]

64. Litjens, G.; Kooi, T.; Bejnordi, B.E.; Setio, A.A.A.; Ciompi, F.; Ghafoorian, M.; van der Laak, J.A.W.M.; van Ginneken, B. A survey on deep learning in medical image analysis. *Med. Image Anal.* **2017**, *42*, 60–88. [CrossRef] [PubMed]

65. Aishwarya, T.; Kumar, V.R. Machine Learning and Deep Learning Approaches to Analyze and Detect COVID-19: A Review. *SN Comput. Sci.* **2021**, *2*, 226. [CrossRef] [PubMed]

66. Ismael, A.M.; Şengür, A. Deep learning approaches for COVID-19 detection based on chest X-ray images. *Expert Syst. Appl.* **2021**, *164*, 114054. [CrossRef] [PubMed]

67. Chandra, T.B.; Verma, K.; Singh, B.K.; Jain, D.; Netam, S.S. Coronavirus disease (COVID-19) detection in Chest X-Ray images using majority voting based classifier ensemble. *Expert Syst. Appl.* **2021**, *165*, 113909. [CrossRef] [PubMed]

68. Jiang, H.; Tang, S.; Liu, W.; Zhang, Y. Deep learning for COVID-19 chest CT (computed tomography) image analysis: A lesson from lung cancer. *Comput. Struct. Biotechnol. J.* **2021**, *19*, 1391–1399. [CrossRef]

69. Tan, W.; Liu, P.; Li, X.; Liu, Y.; Zhou, Q.; Chen, C.; Gong, Z.; Yin, X.; Zhang, Y. Classification of COVID-19 pneumonia from chest CT images based on reconstructed super-resolution images and VGG neural network. *Health Inf. Sci. Syst.* **2021**, *9*, 10. [CrossRef] [PubMed]

70. Shah, V.; Keniya, R.; Shridharani, A.; Punjabi, M.; Shah, J.; Mehendale, N. Diagnosis of COVID-19 using CT scan images and deep learning techniques. *Emerg. Radiol.* **2021**, *28*, 497–505. [CrossRef]

71. Saha, P.; Mukherjee, D.; Singh, P.K.; Ahmadian, A.; Ferrara, M.; Sarkar, R. GraphCovidNet: A graph neural network based model for detecting COVID-19 from CT scans and X-rays of chest. *Sci. Rep.* **2021**, *11*, 8304. [CrossRef]

72. Alghamdi, H.S.; Amoudi, G.; Elhag, S.; Saeedi, K.; Nasser, J. Deep Learning Approaches for Detecting COVID-19 From Chest X-ray Images: A Survey. *IEEE Access* **2021**, *9*, 20235–20254. [CrossRef]

73. Ozsahin, I.; Sekeroglu, B.; Musa, M.S.; Mustapha, M.T.; Ozsahin, D.U. Review on Diagnosis of COVID-19 from Chest CT Images Using Artificial Intelligence. *Comput. Math. Methods Med.* **2020**, *2020*, 9756518. [CrossRef] [PubMed]

74. Rahman, S.; Sarker, S.; Miraj, M.A.A.; Nihal, R.A.; Haque, A.K.M.N.; Noman, A.A. Deep Learning-Driven Automated Detection of COVID-19 from Radiography Images: A Comparative Analysis. *Cogn. Comput.* **2021**. [CrossRef]

75. Bhattacharya, S.; Maddikunta, P.K.R.; Pham, Q.V.; Gadekallu, T.R.; Krishnan, S.R.; Chowdhary, C.L.; Alazab, M.; Pirand, J. Deep learning and medical image processing for coronavirus (COVID-19) pandemic: A survey. *Sustain. Cities Soc.* **2021**, *65*, 102589. [CrossRef]

76. Roberts, M.; Driggs, D.; Thorpe, M.; Gilbey, J.; Yeung, M.; Ursprung, S.; Aviles-Rivero, A.I.; Etmann, C.; McCague, C.; Beer, L.; et al. Common pitfalls and recommendations for using machine learning to detect and prognosticate for COVID-19 using chest radiographs and CT scans. *Nat. Mach. Intell.* **2021**, *3*, 199–217. [CrossRef]

77. Shuja, J.; Alanazi, E.; Alasmary, W.; Alashaikh, A. COVID-19 open source data sets: A comprehensive survey. *Appl. Intell.* **2021**, *51*, 1296–1325. [CrossRef]

78. Mohamadou, Y.; Halidou, A.; Kapen, P.T. A review of mathematical modeling, artificial intelligence and datasets used in the study, prediction and management of COVID-19. *Appl. Intell.* **2020**, *50*, 3913–3925. [CrossRef]

79. Vidal, P.L.; de Moura, J.; Novo, J.; Ortega, M. Multi-stage transfer learning for lung segmentation using portable X-ray devices for patients with COVID-19. *Expert Syst. Appl.* **2021**, *173*, 114677. [CrossRef]

80. Yao, Q.; Xiao, L.; Liu, P.; Zhou, S.K. Label-Free Segmentation of COVID-19 Lesions in Lung CT. *IEEE Trans. Med. Imaging* **2021**. [CrossRef]

81. Saood, A.; Hatem, I. COVID-19 lung CT image segmentation using deep learning methods: U-Net versus SegNet. *BMC Med. Imaging* **2021**, *21*, 19. [CrossRef]

82. Fan, D.P.; Zhou, T.; Ji, G.P.; Zhou, Y.; Chen, G.; Fu, H.; Shen, J.; Shao, L. Inf-Net: Automatic COVID-19 Lung Infection Segmentation from CT Images. *IEEE Trans. Med. Imaging* **2020**, *39*, 2626–2637. [CrossRef] [PubMed]

83. Xu, Y.; Lam, H.K.; Jia, G. MANet: A two-stage deep learning method for classification of COVID-19 from chest X-ray images. *Neurocomputing* **2021**, *443*, 96–105. [CrossRef]

84. Kusakunniran, W.; Karnjanapreechakorn, S.; Siriapisith, T.; Borwarnginn, P.; Sutassananon, K.; Tongdee, T.; Saiviroonporn, P. COVID-19 detection and heatmap generation in chest X-ray images. *J. Med. Imaging* **2021**, *8*, 014001. [CrossRef] [PubMed]

85. Elmuogy, S.; Hikal, N.A.; Hassan, E. An efficient technique for CT scan images classification of COVID-19. *J. Intell. Fuzzy Syst.* **2021**, *40*, 5225–5238. [CrossRef]

86. Mishra, A.K.; Das, S.K.; Roy, P.; Bandyopadhyay, S. Identifying COVID19 from Chest CT Images: A Deep Convolutional Neural Networks Based Approach. *J. Healthc. Eng.* **2020**, *2020*, 8843664. [CrossRef]

87. Hussain, E.; Hasan, M.; Rahman, A.; Lee, I.; Tamanna, T.; Parvez, M.Z. CoroDet: A deep learning based classification for COVID-19 detection using chest X-ray images. *Chaos Solitons Fractals* **2021**, *142*, 110495. [CrossRef]

88. Das, A.K.; Ghosh, S.; Thunder, S.; Dutta, R.; Agarwal, S.; Chakrabarti, A. Automatic COVID-19 detection from X-ray images using ensemble learning with convolutional neural network. *Pattern Anal. Appl.* **2021**, *24*, 1111–1124. [CrossRef]

89. Xu, J.; Xiang, L.; Liu, Q.; Gilmore, H.; Wu, J.; Tang, J.; Madabhushi, A. Stacked Sparse Autoencoder (SSAE) for Nuclei Detection on Breast Cancer Histopathology Images. *IEEE Trans. Med. Imaging* **2016**, *35*, 119–130. Data Availability Statement: [CrossRef]

90. Chen, M.; Shi, X.; Zhang, Y.; Wu, D.; Guizani, M. Deep Features Learning for Medical Image Analysis with Convolutional Autoencoder Neural Network. *IEEE Trans. Big Data* **2017**, *7*, 750–758. [CrossRef]

91. Li, D.; Fu, Z.; Xu, J. Stacked-autoencoder-based model for COVID-19 diagnosis on CT images. *Appl. Intell.* **2020**, *51*, 2805–2817. [CrossRef]

92. Hanafi, H.; Pranolo, A.; Mao, Y. CAE-COVIDX: Automatic COVID-19 disease detection based on X-ray images using enhanced deep convolutional and autoencoder. *Int. J. Adv. Intell. Inform.* **2021**, *7*, 49–62. [CrossRef]

93. Aung, D.M.; Yuzana. Coronavirus Disease (COVID-19) Detection System using Histogram Oriented Gradients and Feed Forward Neural Network. *J. Comput. Appl. Res.* **2020**, *1*, 217–220.

94. Siracusano, G.; La Corte, A.; Gaeta, M.; Cicero, G.; Chiappini, M.; Finocchio, G. Pipeline for Advanced Contrast Enhancement (PACE) of Chest X-ray in Evaluating COVID-19 Patients by Combining Bidimensional Empirical Mode Decomposition and Contrast Limited Adaptive Histogram Equalization (CLAHE). *Sustainability* **2020**, *12*, 8573. [CrossRef]

95. Javed, R.; Rahim, M.S.M.; Saba, T.; Fati, S.M.; Rehman, A.; Tariq, U. Statistical Histogram Decision Based Contrast Categorization of Skin Lesion Datasets Dermoscopic Images. *Comput. Mater. Contin.* **2021**, *67*, 2337–2352. [CrossRef]

96. Hussain, M.A.; Hamarneh, G.; Garbi, R. ImHistNet: Learnable Image Histogram Based DNN with Application to Noninvasive Determination of Carcinoma Grades in CT Scans. In Proceedings of the International Conference on Medical Image Computing and Computer-Assisted Intervention (MICCAI 2019), Shenzhen, China, 13–17 October 2019; Volume 11769, pp. 130–138. [CrossRef]

97. Ruiz, E.; Ramírez, J.; Górriz, J.M.; Casillas, J. Alzheimer's Disease Computer-Aided Diagnosis: Histogram-Based Analysis of Regional MRI Volumes for Feature Selection and Classification. *J. Alzheimer's Dis.* **2018**, *65*, 819–842. [CrossRef]

98. Pereira, P.M.M.; Tavora, L.M.M.; Fonseca-Pinto, R.; Paiva, R.; Assunção, P.; Faria, S. Image Segmentation using Gradient-based Histogram Thresholding for Skin Lesion Delineation. In Proceedings of the 6th International Conference on Biomedical Engeering Systems and Technologies, Prague, Czech Republic, 22–24 February 2019; pp. 84–91. [CrossRef]

99. Thamizhvani, T.R.; Hemalatha, R.H.; Babu, B.; Dhivya, J.A.; Joseph, J.E.; Chandrasekaran, R. Identification of Skin Tumours using Statistical and Histogram Based Features. *J. Clin. Diagn. Res.* **2018**, *12*, LC11–LC15. [CrossRef]

100. Wang, Z.; Li, H.; Ouyang, W.; Wang, X. Learnable Histogram: Statistical Context Features for Deep Neural Networks. In Proceedings of the European Conference on Computer Vision (ECCV 2016), Amsterdam, The Netherlands, 11–14 October 2016; pp. 246–262. [CrossRef]

101. Rundo, L.; Tangherloni, A.; Cazzaniga, P.; Nobile, M.S.; Russo, G.; Gilardi, M.C.; Vitabile, S.; Mauri, G.; Besozzi, D.; Militello, C. A novel framework for MR image segmentation and quantification by using MedGA. *Comput. Methods Programs Biomed.* **2019**, *176*, 159–172. [CrossRef]

102. Acharya, U.K.; Kumar, S. Particle swarm optimized texture based histogram equalization (PSOTHE) for MRI brain image enhancement. *Optik* **2020**, *224*, 165760. [CrossRef]

103. Romanov, A.; Bach, M.; Yang, S.; Franzeck, F.C.; Sommer, G.; Anastasopoulos, C.; Bremerich, J.; Stieltjes, B.; Weikert, T.; Sauter, A.W. Automated CT Lung Density Analysis of Viral Pneumonia and Healthy Lungs Using Deep Learning-Based Segmentation, Histograms and HU Thresholds. *Diagnostics* **2021**, *11*, 738. [CrossRef]

104. Swain, M.J.; Ballard, D.H. Color indexing. *Int. J. Comput. Vis.* **1991**, *7*, 11–32. [CrossRef]

105. Schiele, B.; Crowley, J.L. Probabilistic object recognition using multidimensional receptive field histograms. In Proceedings of the European Conference on Computer Vision, Vienna, Austria, 25–29 August 1996; pp. 610–619.

106. Kullback, S. *Information Theory and Statistics*; Dover Pubns: Mineola, NY, USA, 1997.

107. Bhattacharyya, A. On a measure of divergence between two statistical populations defined by probability distributions. *Bull. Calcutta Math. Soc.* **1943**, *35*, 99–109.

108. Gunraj, H.; Wang, L.; Wong, A. COVIDNet-CT: A Tailored Deep Convolutional Neural Network Design for Detection of COVID-19 Cases From Chest CT Images. *Front. Med.* **2020**, *7*, 608525. [CrossRef]

109. Gunraj, H.; Sabri, A.; Koff, D.; Wong, A. COVID-Net CT-2: Enhanced Deep Neural Networks for Detection of COVID-19 from Chest CT Images Through Bigger, More Diverse Learning. *arXiv* **2021**, arXiv:2101.07433.

110. Alpaydin, E. *Introduction to Machine Learning*, 3rd ed.; Mit Press: Cambridge, MA, USA, 2014.

111. Krizhevsky, A.; Sutskever, I.; Hinton, G.E. ImageNet Classification with Deep Convolutional Neural Networks. In Proceedings of the 26th International Conference on Neural Information Processing Systems, Lake Tahoe, NV, USA, 3–8 December 2012; pp. 1097–1105. [CrossRef]

112. Szegedy, C.; Liu, W.; Jia, Y.; Sermanet, P.; Reed, S.; Anguelov, D.; Erhan, D.; Vanhoucke, V.; Rabinovich, A. Going deeper with convolutions. In Proceedings of the 2015 IEEE Conference on Computer Vision and Pattern Recognition (CVPR), Boston, MA, USA, 7–12 June 2015. [CrossRef]

113. He, K.; Zhang, X.; Ren, S.; Sun, J. Deep residual learning for image recognition. In Proceedings of the IEEE Conference on Computer Vision and Pattern Recognition (CVPR 2016), Las Vegas, NV, USA, 27–30 June 2016; pp. 770–778. [CrossRef]

114. Kingma, D.P.; Ba, J. Adam: A Method for Stochastic Optimization. In Proceedings of the 3rd International Conference for Learning Representations (ICLR 2015), San Diego, CA, USA, 7–9 May 2015; pp. 1–15.

115. Rubner, Y.; Tomasi, C.; Guibas, L.J. The earth mover's distance as a metric for image retrieval. *Int. J. Comput. Vis.* **2000**, *40*, 99–121. [CrossRef]

116. Baccarelli, E.; Vinueza Naranjo, P.G.; Shojafar, M.; Scarpiniti, M. Q*: Energy and Delay-efficient Dynamic Queue Management in TCP/IP Virtualized Data Centers. *Comput. Commun.* **2017**, *102*, 89–106. [CrossRef]

117. Baccarelli, E.; Scarpiniti, M.; Momenzadeh, A.; Sarv Ahrabi, S. Learning-in-the-Fog (LiFo): Deep Learning meets Fog Computing for the Minimum-Energy Distributed Early-Exit of Inference in delay-critical IoT realms. *IEEE Access* **2021**, *9*, 2571–25757. [CrossRef]

118. Baccarelli, E.; Biagi, M. Optimized Power Allocation and Signal Shaping for Interference-Limited Multi-antenna "Ad Hoc" Networks. In *Personal Wireless Communications. PWC 2003*; Lecture Notes in Computer Science; Conti, M., Giordano, S., Gregori, E., Olariu, S., Eds.; Springer: Berlin, Germany, 2003; Volume 2775, pp. 138–152. [CrossRef]

119. Baccarelli, E.; Biagi, M.; Pelizzoni, C. On the Information Throughput and optimized Power Allocation for MIMO Wireless Systems with imperfect channel Estimate. *IEEE Trans. Signal Process.* **2005**, *53*, 2335–2347. [CrossRef]

120. Baccarelli, E.; Biagi, M.; Bruno, R.; Conti, M.; Gregori, E. Broadband Wireless Access Networks: A Roadmap on Emerging Trends and Standards. In *Broadband Services: Business Models and Technologies for Community Networks*; Wiley Online Library: Chichester, UK, 2005; Chapter 14, pp. 215–240. [CrossRef]